Supplemental Materials

Molecular Biology of the Cell

Nickaeen *et al*.

Supplemental Text

Model and results: mathematical details

1. Nucleation and polymerization kinetics and transport of actin.

The model combines detailed kinetics of actin nucleation and polymerization (Berro et al., 2010) and mechanics of actin filament meshwork approximated as a visco-active gel (Kruse et al., 2005). It is formulated in a continuous approximation that does not resolve individual filaments, but rather describes a distribution of actin in the patch by a continuous density of polymerized subunits ρ as a function of spatial location $\mathbf{r}$ and time t, $\rho(\mathbf{r},t)$. The actin density ρ is determined by concentrations of all of the species of actin in an actin patch including the newly polymerized ATP-bound subunits (FATP), the subunits aged by ATP hydrolysis and phosphate dissociation (FADP), the subunits bound by cofilin (FCOF), the filaments barbed-ends, both active and capped (BEa and BEc, respectively), and the slowly depolymerizing pointed ends (PE): $\rho = n_A \sum_X [X]$, where X stands for FATP, FADP, FCOF, BEa, BEc, and PE; $[X]$ is the concentration of molecule X in μM; the prefactor n_A converts the concentration in μM into the density expressed in molecules per μm^3 ($n_A = 602$ $\mu m^{-3}/\mu M$).

The concentrations $[X]$ are governed by transport-reaction equations of the following type,

$$\partial_t [X] = -\nabla \cdot (\mathbf{v} \cdot [X]) + R_X . \qquad \text{(S1)}$$

The first term in Eq (S1) is the rate of change of $[X]$ due to advective flow of actin meshwork characterized by the vector field of local time-dependent velocities $\mathbf{v} = \mathbf{v}(\mathbf{r},t)$. Like $[X]$ and surface densities $[Y]$ of actin-nucleating species (see below), actin velocities $\mathbf{v}(\mathbf{r},t)$ are the model variables; they are governed by the mechanics of actin filament meshwork described in the next section. The second term in Eq (S1) is the sum of rates of all reactions affecting a given X. The wiring schematic of reactions involved in nucleation, polymerization, and severing of actin, and capping of the barbed ends of actin filaments is shown in Figure S1. The diagram includes two more volume species that do not directly contribute to $\rho(\mathbf{r},t)$: the active Arp2/3 complex (ActiveArp) and the Arp2/3 complex in the filamentous actin network (FArp). While the equation governing FArp is of the form of Eq (S1), the equation for ActiveArp has an additional diffusion term:

$$\partial_t [\text{ActiveArp}] = \nabla \cdot \big(D(\mathbf{r}) \nabla([\text{ActiveArp}]\big) - \mathbf{v}[\text{ActiveArp}]) + R_{\text{ActiveArp}} , \qquad \text{(S1*)}$$

where $D(\mathbf{r})$ is nonzero only in the vicinity of the rings of nucleation promoting factors (NPFs), as described in the next section (for reasoning and details, see (Nickaeen et al., 2019)).

Reaction steps leading to formation of ActiveArp occur on the surface of the membrane, where they localize to the rings occupied by the nucleation promoting factors WASp (Figure S1). They involve dimers of WASp bound to G-actin monomers (WGD), Arp2/3 ternary complexes

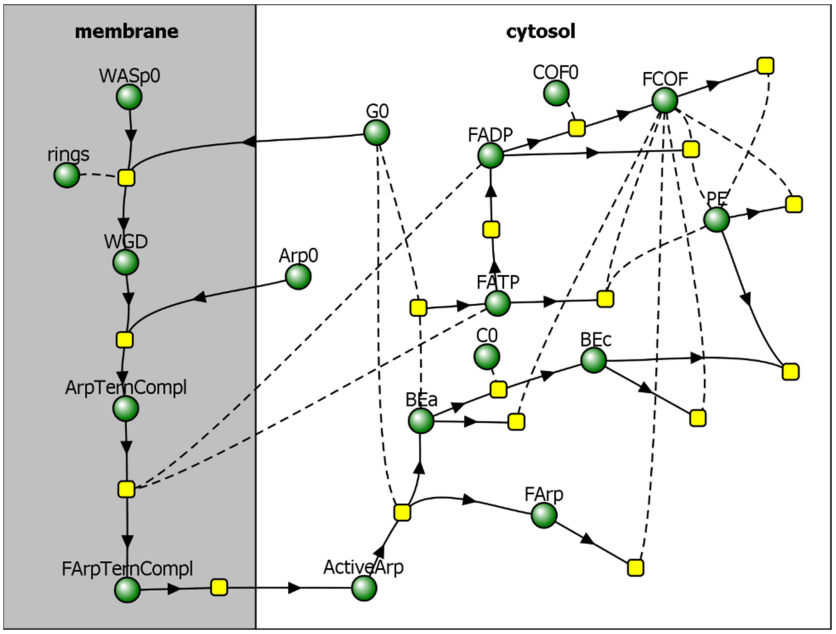

Figure S1. Reaction diagram of nucleation and polymerization of patch actin proposed in (Berro et al., 2010), with added partitioning of species between membrane and cytosol (adapted from (Nickaeen et al., 2019)). Directions of arrows towards or from reaction nodes (yellow squares) determine roles of molecular species (green circles) in a particular reaction as reactants or products, and reactions without products describe disappearance of reactants from the patch. Species connected to reactions by dashed curves act as 'catalysts', i.e. they are not consumed in those reactions.

consisting of Arp2/3 complex bound to WGD (ArpTernCompl), and activated Arp2/3 ternary complexes (FArpTernCompl), whose surface densities are described by rate equations,

$$\partial_t [Y] = R_Y \,, \qquad \text{(S1**)}$$

where $[Y]$ is the surface density of a membrane-bound protein Y in molecules per squared micron. Note that while these variables are governed by ordinary differential equations, they also depend on spatial coordinates, given that R_Y are nonzero at the rings occupied by WASp, and $R_{\text{ArpTernCompl}}$ depends on [FATP] and [FADP] at the plasma membrane.

Reaction rates structure in R_X and R_Y are as in (Berro et al., 2010). The on (+) and off (-) rate constants of polymerization, capping, cofilin binding, and cofilin-dependent severing from (Berro et al., 2010) were modified by the factor $\alpha(\mathbf{r},t) = (1-\rho(\mathbf{r},t)/\rho_{\max})^{1/2}$, to reflect the effect of molecular crowding; and the rates of polymerization and capping were modified by an additional factor $\beta(\mathbf{r},t) = 1-\rho(\mathbf{r},t)/\rho_{\max}$, to take into account that polymerization and capping slow down under load, where $\rho_{\max} = (4\pi\delta^3/3)^{-1}$ (δ is the length of actin subunit; for derivation details, see (Nickaeen et al., 2019)). The expressions of R_X and R_Y used in computations are shown below:

$$R_{\mathrm{BEa}} = \alpha\{\beta k^{+}_{\mathrm{Polymerization}} \mathrm{G}_0[\mathrm{ActiveArp}] + k^{-}_{\mathrm{Cap}}[\mathrm{BEc}] - (\beta k^{+}_{\mathrm{Cap}} \mathrm{C}_0 + k_{\mathrm{Chop}}[\mathrm{FCOF}]) \cdot [\mathrm{BEa}]\}$$

$$R_{\mathrm{BEc}} = \alpha\{\beta k^{+}_{\mathrm{Cap}}[\mathrm{BEc}] - (k^{-}_{\mathrm{Cap}} + k_{\mathrm{Chop}}[\mathrm{FCOF}] + k^{-}_{\mathrm{Depolymerization}}[\mathrm{PE}]/[\mathrm{F_{tot}}]) \cdot [\mathrm{BEc}]\}$$

$$R_{\mathrm{PE}} = \alpha\{-(k_{\mathrm{Chop}}[\mathrm{FCOF}] + k^{-}_{\mathrm{Depolymerization}}[\mathrm{BEc}]/[\mathrm{F_{tot}}]) \cdot [\mathrm{PE}]\}$$

$$R_{\mathrm{FADP}} = k_{\mathrm{Hydrolysis}} \cdot [\mathrm{FATP}] + \alpha k^{-}_{\mathrm{COFBinding}} \cdot [\mathrm{FCOF}]$$
$$- \alpha(k^{+}_{\mathrm{COFBinding}} \cdot \mathrm{COF}_0 + k_{\mathrm{Chop}}[\mathrm{FCOF}] + k^{-}_{\mathrm{Depolymerization}}[\mathrm{PE}]/[\mathrm{F_{tot}}]) \cdot [\mathrm{FADP}]$$

$$R_{\mathrm{FCOF}} = \alpha\{k^{+}_{\mathrm{COFBinding}} \cdot \mathrm{COF}_0[\mathrm{FADP}] - (k^{-}_{\mathrm{COFBinding}} + k_{\mathrm{Chop}}[\mathrm{FCOF}] + k^{-}_{\mathrm{Depolymerization}}[\mathrm{PE}]/[\mathrm{F_{tot}}]) \cdot [\mathrm{FCOF}]\}$$

$$R_{\mathrm{ActiveArp}} = -\alpha\beta k^{+}_{\mathrm{Polymerization}} \mathrm{G}_0[\mathrm{ActiveArp}]$$

$$R_{\mathrm{FArp}} = \alpha\{\beta k^{+}_{\mathrm{Polymerization}} \mathrm{G}_0[\mathrm{ActiveArp}] - k_{\mathrm{Chop}}[\mathrm{FCOF}]) \cdot [\mathrm{FArp}]\}$$

$$R_{\mathrm{WGD}} = k^{+}_{\mathrm{WASpGBinding}} \mathrm{G}_0 \mathrm{WASp}_0 \exp((t - t_{\mathrm{peak}})^2 / \sigma) + k^{-}_{\mathrm{ArpComplFormation}}[\mathrm{ArpTernCompl}]$$
$$- (k^{-}_{\mathrm{WASpGBinding}} + k^{+}_{\mathrm{ArpComplFormation}} \mathrm{Arp}_0)[\mathrm{WGD}]$$

$$R_{\mathrm{ArpTernCompl}} = k^{+}_{\mathrm{ArpComplFormation}} \mathrm{Arp}_0 \mathrm{WGD} - (k^{-}_{\mathrm{ArpComplFormation}} + k^{+}_{\mathrm{ArpGWBinding}}([\mathrm{FATP}] + [\mathrm{FADP}]))[\mathrm{ArpTernCompl}]$$

$$R_{\mathrm{FATP}} = \alpha\beta k^{+}_{\mathrm{Polymerization}}[\mathrm{BEa}] - (k_{\mathrm{Hydrolysis}} + \alpha k_{\mathrm{Chop}}[\mathrm{FCOF}] + \alpha k^{-}_{\mathrm{Depolymerization}}[\mathrm{PE}]/[\mathrm{F_{tot}}]) \cdot [\mathrm{FATP}]$$

$$R_{\mathrm{ArpTernCom\,pl}} = k^{+}_{\mathrm{ArpGWBindi\,ng}}([\mathrm{FATP}] + [\mathrm{FADP}])[\mathrm{ArpTernCom\,pl}] - k^{+}_{\mathrm{ArpActivat\,ion}}[\mathrm{FArpTernCo\,mpl}]$$

In the expressions above, $\mathrm{F_{tot}} = \rho / n_A = [\mathrm{FATP}] + [\mathrm{FADP}] + [\mathrm{FCOF}] + [\mathrm{BEa}] + [\mathrm{BEc}] + [\mathrm{PE}]$ and the zero subscript denotes constant concentrations and surface density. Table S1 summarizes the values of constants used in the reaction rate expressions and initial conditions for Eqs (1) and for the rate equations describing actin nucleation. For their sources, see Tables 1 and 2 of (Berro et al., 2010). Table S1 also includes the constants involved in actin mechanics: the actin subunit length δ and the constants κ_{active} and $\kappa_{\mathrm{viscous}}$ setting the scales of active and viscous stress and of actin velocities; for derivation of κ_{active} and $\kappa_{\mathrm{viscous}}$, see (Nickaeen et al., 2019).

2. Mechanics of actin meshwork.

We interpret mechanics of actin meshwork as that of a compressible visco-active fluid (Kruse et al., 2005; Prost et al., 2015). In a viscosity-dominated environment of the actin patch, actin velocities $\mathbf{v}(\mathbf{r},t)$ are governed by the balance of local active and viscous forces (per unit volume), $\mathbf{f}_{\mathrm{active}}$ and $\mathbf{f}_{\mathrm{viscous}}$ (Kruse et al., 2005):

$$\underbrace{\nabla \cdot \hat{\boldsymbol{\sigma}}_{\mathrm{viscous}}}_{\mathbf{f}_{\mathrm{viscous}}(\mathbf{r},t)} + \underbrace{\nabla \cdot \hat{\boldsymbol{\sigma}}_{\mathrm{active}}}_{\mathbf{f}_{\mathrm{active}}(\mathbf{r},t)} = 0\,, \qquad \text{(S2)}$$

where $\hat{\boldsymbol{\sigma}}_{\mathrm{viscous}} = \eta(\rho, L)(\nabla\mathbf{v} + (\nabla\mathbf{v})^T)$ and $\hat{\boldsymbol{\sigma}}_{\mathrm{active}} = \sigma_a(\rho)\hat{\mathbf{I}}$ are the viscous and active stress tensors, respectively ($\hat{\mathbf{I}}$ is the unit tensor). In the expression for the viscous stress tensor, $(\nabla\mathbf{v})^T$ is the transpose of the velocity gradient tensor $\nabla\mathbf{v}$, and $L = L(\mathbf{r},t)$ is the local average length of

actin filaments, computed as $N\delta$, with the number of subunits in a filament $N = N(\mathbf{r},t) = [\mathrm{F_{tot}}]/([\mathrm{BEa}]+[\mathrm{BEc}])$; $\eta(\rho,L)$ is the dynamic viscosity of the actin filament meshwork, and $\sigma_a(\rho)$ is the energy (per unit volume) stored in the meshwork during polymerization. By analyzing rheological properties of overlapping actin filaments (Gardel et al., 2003; Kasza et al., 2010; Tseng and Wirtz, 2004; Mullins et al., 1998), we derived the following constitutive relations for $\eta(\rho,L)$ and $\sigma_a(\rho)$:

Table S1. Model parameters

Parameter	Value	Units
$k^+_{\mathrm{ArpActivation}}$	0.5	s^{-1}
$k^+_{\mathrm{ArpComplFormation}}$	0.8	$\mu\mathrm{M}^{-1}\mathrm{s}^{-1}$
$k^-_{\mathrm{ArpComplFormation}}$	0.74	s^{-1}
$k^+_{\mathrm{ArpGWBinding}}$	0.3	$\mu\mathrm{M}^{-1}\mathrm{s}^{-1}$
$k^-_{\mathrm{ArpGWBinding}}$	0.001	s^{-1}
k^+_{Cap}	7	$\mu\mathrm{M}^{-1}\mathrm{s}^{-1}$
k^-_{Cap}	0.004	s^{-1}
$k^+_{\mathrm{COFBinding}}$	0.0085	$\mu\mathrm{M}^{-1}\mathrm{s}^{-1}$
$k^-_{\mathrm{COFBinding}}$	0.005	s^{-1}
$k^+_{\mathrm{Polymerization}}$	11.6	$\mu\mathrm{M}^{-1}\mathrm{s}^{-1}$
$k^-_{\mathrm{Depolymerization}}$	0.25	s^{-1}
$k^+_{\mathrm{WASpGWBinding}}$	42.9	$\mu\mathrm{M}^{-1}\mathrm{s}^{-1}$
$k^-_{\mathrm{WASpGWBinding}}$	25.7	s^{-1}
k_{Chop}	0.003	$\mu\mathrm{M}^{-1}\mathrm{s}^{-1}$
$k_{\mathrm{Hydrolysis}}$	0.3	s^{-1}
Arp_0	1.3	$\mu\mathrm{M}$
C_0	0.8	$\mu\mathrm{M}$
COF_0	40	$\mu\mathrm{M}$
G_0	21.6	$\mu\mathrm{M}$
WASp_0	5192*	$\mathrm{molecules}/\mu\mathrm{m}^2$
$t_{\mathrm{peak\ NPF}}$	17.2**	s
σ	33.5	s^2
κ_{active}	$3.69\times10^{-3}n_A^{-2}$	$\mathrm{Pa}/(\mu\mathrm{M})^2$
$\kappa_{\mathrm{viscous}}$	$3.93n_A^{-2}$	$\mathrm{Pa}\cdot\mathrm{s}/\mu\mathrm{M}$
δ	2.7	nm

* Maximum surface density of free WASp in the rings is the number of WASp molecules, that corresponds to concentration 0.23 μM in a sphere of radius 0.15 μm (Berro et al., 2010), divided by area of two rings, $4\pi r_{\mathrm{neck}}w$, where w is the width of one ring. The value is shown for $w = 5$ nm, used in all simulations, and $r_{\mathrm{neck}} = 3$ nm (some simulations were run with neck radii of 6 and 10 nm).

** Upon offsetting by -20 s, $t_{\mathrm{peak\ NPF}}$ becomes -2.8 s (Berro et al., 2010).

$$\eta(\rho, L) = \kappa_{\text{viscous}}\, \rho \cdot (1/N + \rho\delta^2 L) \quad ; \qquad \text{(S3)}$$
$$\sigma_a(\rho) = \kappa_{\text{active}}\, \rho^2$$

note that under the filament overlapping condition $(\rho N^2)^{1/3}\delta > 1$ (Doi and Edwards, 1998), the equations (S3) describing actin viscosity crosses from a linear dependence on ρ over to $\eta \propto \rho^2 L$ (Nickaeen et al., 2019).

3. Computation domain, boundary and initial conditions.

Equations (S1), (S1*), and (S2) are to be solved in a section of the cell embedding a head-neck invagination, see the diagram of a 3D computational domain Ω in Figure S2A (drawn not to scale). The domain is bounded by the plasma membrane $\partial\Omega_{\text{membrane}}$, which includes the invagination, and two additional surfaces that define its vertical cylindrical sides and the horizontal floor. In order for the conditions at the outer limits of the domain, which are arbitrary, to not have significant effect on the results, we solved the model in a sufficiently large, 0.5 μm in each coordinate direction, neighborhood of the invagination. Note that because the invaginated portion of the domain boundary can move, the shape of the computational domain generally changes with time.

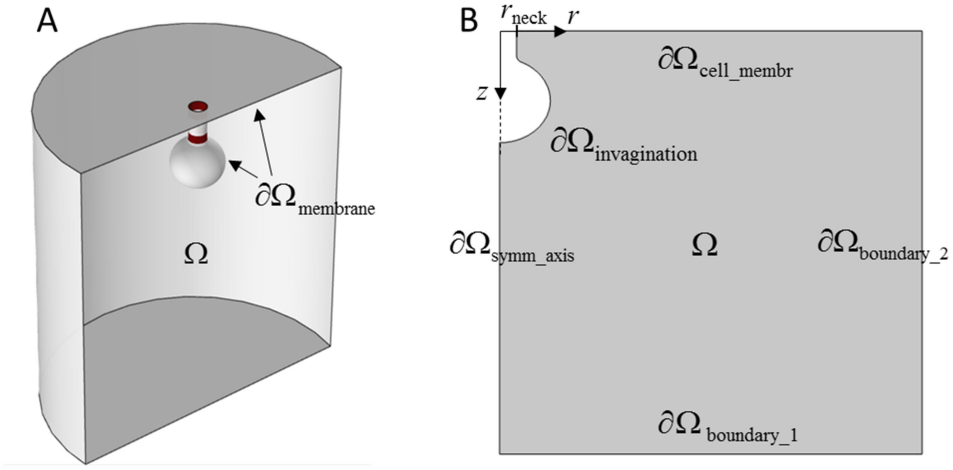

Figure S2. Computational domain. (A) 3D diagram of the fragments of cell, Ω, and plasma membrane, including invagination, $\partial\Omega_{\text{membrane}}$, comprising computational domain (not to scale). Two rings of NPFs are shown in dark red. When invagination elongates, both $\partial\Omega_{\text{membrane}}$ and Ω change with time. (B) Computational domain of the equivalent 2D problem in (r, z) coordinates (not to scale). The domain boundary $\partial\Omega$ includes: fragment of cell membrane $\partial\Omega_{\text{cell\_membr}}$, invagination $\partial\Omega_{\text{invagination}}$, fragment of axis of symmetry, $\partial\Omega_{\text{symm\_axis}}$, and horizontal ($\partial\Omega_{\text{boundary\_1}}$) and vertical ($\partial\Omega_{\text{boundary\_2}}$) outer boundaries; $\partial\Omega_{\text{membrane}} = \partial\Omega_{\text{cell\_membr}} \cup \partial\Omega_{\text{invagination}}$.

Because the model geometry, localization of membrane-bound species, and corresponding fluxes remain axisymmetric throughout the elongation process, solutions of the model are also axisymmetric. This reduces the problem to solving an equivalent 2D model in cylindrical

coordinates (r,z) in the domain Ω depicted Figure S2B (not to scale). The full 3D geometry is then restored for any time by revolving the 2D domain Ω around the axis of symmetry $r=0$.

The equations (S1) for all volume variables, except for [ActiveArp], are of the hyperbolic type and subject to zero-flux boundary conditions at $\partial\Omega_{\text{cell\_membr}} \cup \partial\Omega_{\text{invagination}} \cup \partial\Omega_{\text{symm\_axis}}$ (Figure S2B). For implementation details, see Supplemental Text of (Nickaeen et al., 2019).

Eq (S1*), governing [ActiveArp], is of the parabolic type, because it includes a diffusion term. Therefore, boundary conditions for this equation must be specified at all boundaries in Figure S2B. At $\partial\Omega_{\text{invaginati on}}$, it must satisfy the Rankine-Hugoniot boundary condition (Novak and Slepchenko, 2014),

$$D(r,z)\cdot\partial_r[\text{ActiveArp}] + k^+_{\text{ArpActivation}}[\text{FArpTernCompl}]\,|_{\gamma_{\text{rings}}} = 0,$$

where γ_{rings} are the locations on $\partial\Omega_{\text{invagination}}$ occupied by the rings of the NPFs. Recall that in the equation above, [ActiveArp] is measured in μM, whereas [FArpTernCompl] is in molecules per squared micron. Note also the disappearance of the advection term from the boundary condition, which is due to the no-slip boundary condition for Eq (S2) that we describe later in this section.

The diffusion coefficient of [ActiveArp] $D(r,z)$ is defined as follows:

$$D(r,z) = \begin{cases} D_{AA}\exp(-|\,r - r_{\text{neck}}\,|/\xi), \text{if } (r_{\text{neck}},z) \in \partial\Omega_{\text{invagination}} \\ 0, \text{ otherwise} \end{cases},$$

with $D_{AA} = 0.001$ μm^2/s and $\xi = 3$ nm. The value of ξ is on the order of mesh sizes used in the computations; this parameter has little effect on the solution, because ActiveArp quickly converts to BEa. Because $D(r,z)$ is nonzero only in the tight space near the invagination, varying D_{AA} by several orders of magnitude did not change the simulation outcome in any significant way.

The boundary conditions for [ActiveArp] at $\partial\Omega_{\text{cell\_membr}} \cup \partial\Omega_{\text{symm\_axis}}$ were zero-flux. At the remaining two boundaries, $\partial\Omega_{\text{boundary\_1}}$ and $\partial\Omega_{\text{sboundary\_2}}$, we applied outflow boundary conditions. For reasons explained in Supplemental Text of (Nickaeen et al., 2019), we specified the outflow boundary conditions at $\partial\Omega_{\text{boundary\_1}} \cup \partial\Omega_{\text{boundary\_2}}$ for all volume variables.

Similar to the Stokes equation for a Newtonian fluid, Eq (S2) is elliptic in nature and hence requires that boundary conditions be specified at all boundaries of Ω. At $\partial\Omega_{\text{cell\_membr}}$ and $\partial\Omega_{\text{invagination}}$, we applied the no-slip boundary condition,

$$\mathbf{v}(\mathbf{r},t) = \mathbf{u}(\mathbf{r},t) \;\; (\mathbf{r} \in \partial\Omega_{\text{membrane}}),$$

where the membrane velocity $\mathbf{u}(\mathbf{r},t)$ may be nonzero only for the points of $\partial\Omega_{\text{invagination}}$. In the model, these points move with the same velocity, $\mathbf{u}(t)=(u_r(t),u_z(t))=(0,u(t))$, where $u(t)$ is governed by Eq (1) of the main text. At $\partial\Omega_{\text{symm\_axis}}$, velocities $\mathbf{v}(\mathbf{r},t)$ were set to zero, and at $\partial\Omega_{\text{boundary\_1}}\cup\partial\Omega_{\text{boundary\_2}}$, the velocities satisfied the zero-stress boundary condition: $(\eta(\rho,L)(\nabla\mathbf{v}+(\nabla\mathbf{v})^T)+\sigma_a(\rho)\hat{\mathbf{I}})\cdot\mathbf{n}=0$.

The initial actin velocities and concentrations of all molecular species, except for [FADP], [BEa], and [PE], were set to zero. Small initial values assigned to [FADP], [BEa], and [PE] reflected a small number of seed filaments (Chen and Pollard, 2013).

4. Computation of the driving force.

The elongation rate is determined in our model by the interplay of the driving force $f_{\text{drive}}(t)$ produced by the stresses in the assembling actin patch, and the resistive force $f_{\text{resist}}(t)$ due to turgor pressure (the latter is defined by Eqs (2) and (2*) of the main text). From fluid mechanics, the driving force is found by integrating the viscous and active stress tensors projected on the outward normal (Landau and Lifshitz, 1989),

$$f_{\text{drive}}(t)=\mathbf{e}_z\int_{\partial\Omega_{\text{invagination}}(t)}(\hat{\boldsymbol{\sigma}}_{\text{active}}+\hat{\boldsymbol{\sigma}}_{\text{viscous}})\cdot\mathbf{n}ds\,, \tag{S4}$$

where the integral is carried over the time-dependent invaginated membrane $\partial\Omega_{\text{invagination}}(t)$, $\mathbf{n}=(n_r,n_z)^T$ is the outward unit normal vector to the membrane (directed towards the interior of Ω), $\mathbf{e}_z$ is the unit vector parallel to the axis of symmetry, and ds is the area of an infenitesimal element of the invaginated membrane.

5. Numerical solution of the model.

5.1 Numerical methods

We solved the equivalent 2D model numerically using a moving-mesh solver of COMSOL® Multiphysics (COMSOL Multiphysics, 2015). The solver utilizes Arbitrary Lagrangian Eulerian (ALE) methods based on finite-element (FE) discretization. The ALE methods are described in numerous publications, see e.g. (Donea et al., 2004).

In an ALE simulation, the computational grid points move with the velocities defined as follows. At the moving interfaces, they coincide with the velocities of the points of the interface. In the interior of the domain, the velocities of the grid are arbitrary, so long as they comprise the smooth vector field that would maintain mesh quality throughout the simulation, while preserving mesh connectivity. Correspondingly, the governing equations formulated with respect to a fixed (Eulerian) coordinate system should be reformulated based on the ALE methodology. For the implementation of our model in the ALE framework and details of its FE formulation, see the supplemental material of (Nickaeen et al., 2019).

5.2 Nonlinear solver, time stepper, and computational mesh

The coupled nonlinear system of equations describing the cytoplasmic species, Eqs (S1, S*), the membrane-bound species, Eqs (S1**), the ring's position, Eq (1) of the main text, and the actin velocities, Eqs (S2), the mesh update equations, along with the corresponding boundary conditions, were discretized using FE mesh and solved in a segregated manner in COMSOL. Details of such a segregated approach can be found elsewhere (Nickaeen et al., 2017; Ferziger and Perić. 2002). Briefly, the solution of the coupled nonlinear system of equations at each time step is broken into 4 consecutive steps: the Mesh update, the cytoplasmic concentrations update, the membrane ODEs update, and the actin velocity update. At each segregated solver's step, we solve equations for a group of variables while treating the coupling terms consisting of other variables using a fixed-point iteration. Each step of the segregated solver may require additional linearization to account for nonlinearities related to the variables that are solved during that step. In these cases, Newton's method with a constant damping factor of 1 was used and the system's Jacobian was updated at each nonlinear iteration. The resulting linearized system was solved monolithically using a direct MUMPS solver with default solver parameters. Once all steps (one cycle) of the segregated solver is completed, the errors are checked and the iterations for additional, if necessary, cycles are performed to achieve the desired convergence criteria.

Note that even though the force-balance equation does not involve time derivatives, the coupled system constitutes an initial-value problem, so that initial conditions must be specified for all variables (initial values of the actin velocities were set to zero). The time-dependent system was solved using a backward-differentiation time-stepping method of order 1-2. Relative and absolute tolerances of the time-stepper were set to 1×10^{-5} and 1×10^{-6}, respectively. Other default solver parameters were used without modification. We verified, by solving the problem with varying solver parameters (including the tolerances of the time-stepper), that the solutions did not depend on specific choices of parameters of the solver.

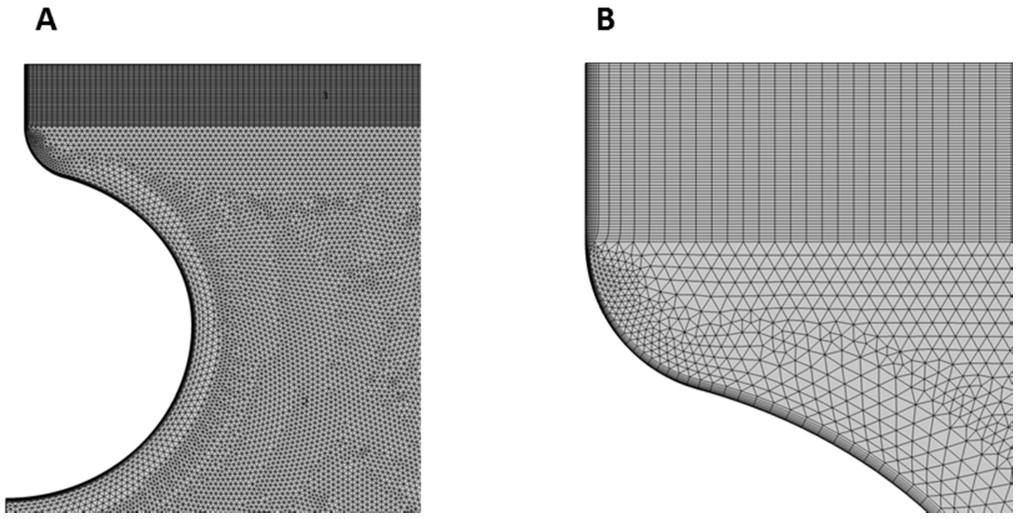

Figure S3. Computational mesh: full view (A), and a zoomed-in view near the boundaries (B).

The computational domain was discretized using hybrid quadrilateral and triangular finite elements (Figure 3A) to accommodate large curvature changes and to allow for sufficient mesh refinement in regions near the invagination in the new head-neck geometry (Figure 3B).

Full details of the numerical implementation of the model can be found in the attached COMSOL Multiphysics file (Figure2.mph). This simulation file corresponds to the head-neck geometry and is set up with parameters corresponding to Figure 2 of the main text.

6. Effects of the timing of resistance reduction on beginning of elongation and maximum driving force.

The timing of the resistance descent t_0 affects the time t_{begin}, at which the invagination begins to elongate, and the magnitude of the driving force at $t = t_{\text{begin}}$. Indeed, t_{begin} satisfies the equaiton $f_{\text{drive}}(t) = f_{\text{resist}}(t)$, so that t_{begin} and $f_{\text{drivel}}(t_{\text{begin}})$ are the coordinates of a point where the graphs

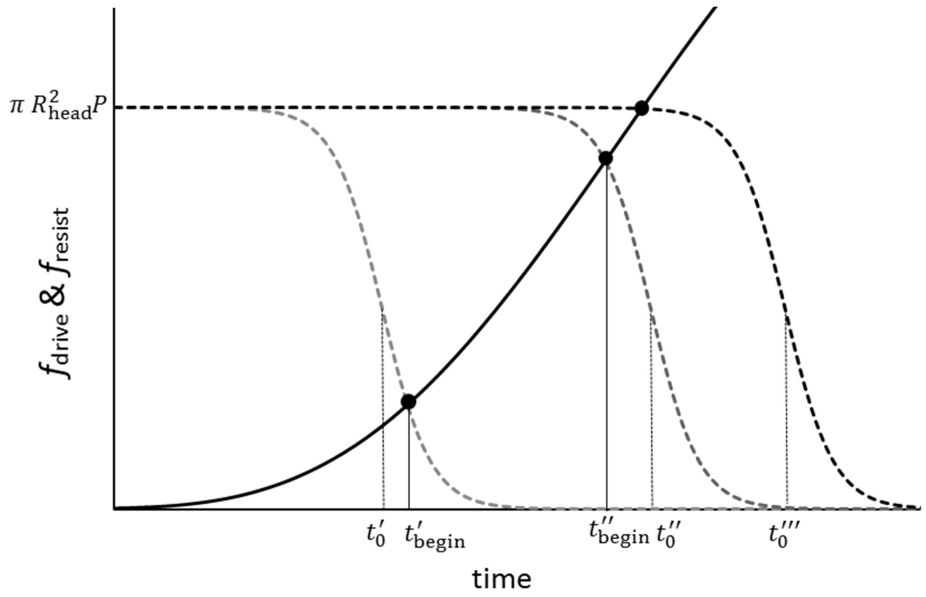

Figure S4. Effects of t_0 on t_{begin} and $f_{\text{drive}}(t_{\text{begin}})$. As t_0 increases, the graph of $f_{\text{resist}}(t)$ (dashed curve) shifts to the right (Eq (2) of the main text), and the coordinates of its intersection with the graph of $f_{\text{drive}}(t)$ (solid curve), t_{begin} and $f_{\text{drive}}(t_{\text{begin}})$, also go up. However, this effect saturates, once the point of intersection reaches the upper plateau of $f_{\text{resist}}(t)$, as is the case with t_0'''; t_0'' is an example of a a 'near-saturation' value of t_0.

of $f_{\text{drive}}(t)$ and $f_{\text{resist}}(t)$ intersect (Figure S4). As t_0 increases, the point of intersection 'slides' up along the graph of $f_{\text{drive}}(t)$, yielding higher t_{begin} and $f_{\text{drive}}(t_{\text{begin}})$. However, the effect saturates, once the point of intersection approaches the upper plateau of $f_{\text{resist}}(t)$, as the 'sliding'

along $f_{\text{drive}}(t)$ slows down and eventually comes to a stop. Thus, the highest $f_{\text{drive}}(t_{\text{begin}})$ is $\pi R_{\text{head}}^2 P$ and $\max(t_{\text{begin}}) = f_{\text{drive}}^{-1}(\pi R_{\text{head}}^2 P)$, where f_{drive}^{-1} denotes the inverse function of $f_{\text{drive}}(t)$. Both limits are controlled by turgor pressure.

The effect of t_0 on t_{begin} and $f_{\text{drive}}(t_{\text{begin}})$ begins to saturate when t_{begin} approaches an inflection point of the rate of change of $f_{\text{resist}}(t)$, as illustrated by t''_{begin} in Figure S4. From Eq (2) of the main text, the respective root t_* of $\partial^3 f_{\text{resist}}(t) = 0$ is the solution of $\exp((t_* - t_0)/\tau) = 2 - \sqrt{3}$, and $f_{\text{drive}}(t_*) = f_{\text{resist}}(t_*) = \pi R_{\text{head}}^2 P/(3 - \sqrt{3})$. Then the 'near-saturation' values of t_0 are $t_0 \approx t_* + \tau \ln(2 + \sqrt{3}) = f_{\text{drive}}^{-1}(\pi R_{\text{head}}^2 P/(3 - \sqrt{3})) + \tau \ln(2 + \sqrt{3})$.

References

Berro, J., V. Sirotkin, and T.D. Pollard. 2010. Mathematical Modeling of Endocytic Actin Patch Kinetics in Fission Yeast: Disassembly Requires Release of Actin Filament Fragments. *Mol. Biol. Cell.* 21: 2905–2915.

COMSOL Multiphysics. 2015. Version 5.2 [software]. Stockholm, Sweden: COMSOL AB. Available from: www.comsol.com.

Chen, Q. and T. D. Pollard. 2013.Actin Filament Severing by Cofilin Dismantles Actin Patches and Produces Mother Filaments for New Patches. *Curr. Biol.* 23:1154-1162.

Doi, M., and S. Edwards. 1998. *The Theory of Polymer Dynamics*, Oxford University Press, New York.

Donea, J., A. Huerta, J.-Ph. Ponthot, and A. Rodriguez-Ferran. Arbitrary Lagrangian–Eulerian Methods. 2004. In Stein, E., R. de Borst, and T.J.R. Hughes (eds) *Encyclopedia of Computational Mechanics*. Volume 1: *Fundamentals*, Chichester: John Wiley & Sons.

Ferziger, J. H., and M. Perić. 2002. Computational Methods for Fluid Dynamics, New York: Springer.

Gardel, M.L., M.T. Valentine, J.C. Crocker, A.R. Bausch, and D.A. Weitz. 2003. Microrheology of entangled F-actin solutions. *Phys. Rev. Lett*. 91:158302.

Kasza, K.E., C.P. Broedersz, G.H. Koenderink, Y.C. Lin, W. Messner, E.A. Millman, F. Nakamura, T.P. Stossel, F.C. MacKintosh, and D.A. Weitz. 2010. Actin Filament Length Tunes Elasticity of Flexibly Cross-Linked Actin Networks. *Biophys J.* 99:1091-1100.

Kruse, K., J-F. Joanny, F. Jülicher, J. Prost, and K. Sekimoto. 2005. Generic theory of active polar gels: a paradigm for cytoskeletal dynamics. *Eur. Phys. J. E* 16:5-16.

Landau, L. D., and E.M. Lifshitz. 1987. *Fluid Mechanics, Vol. 6 (Course of Theoretical Physics)*, Pergamon Press, New York.

Mullins, R. D., J. F. Kelleher, J. Xu, and T. D. Pollard. 1998. Arp2/3 Complex from *Acanthamoeba* Binds Profilin and Cross-links Actin Filaments. *Mol. Biol. Cell* 9:841-852.

Nickaeen, M., J. Berro, T. D. Pollard, and B. M. Slepchenko. 2019. Actin assembly produces sufficient forces for endocytosis in yeast. *Mol. Biol. Cell.* 30: 2014–2024.

Nickaeen M, Novak IL, Pulford S, Rumack A, Brandon J, Slepchenko BM, Mogilner A. 2017. A free-boundary model of a motile cell explains turning behavior. *PLoS Comp. Biol.* 13, e1005862.

Novak, I. L., and B. M. Slepchenko. 2014. A conservative algorithm for parabolic problems in domains with moving boundaries. *J. Comput. Phys.* 270: 203-213.

Prost, J., F. Jülicher, and J-F. Joanny. 2015. Active gel physics. *Nat. Phys*. 11: 111-117.

Tseng, Y., and D. Wirtz. 2004. Dendritic Branching and Homogenization of Actin Networks Mediated by Arp2/3 Complex. *Phys. Rev. Lett*. 93:258104.